PAPER

Cite this: *Nanoscale*, 2015, **7**, 14344

FeO$_x$ and Si nano-dots as dual Li-storage centers bonded with graphene for high performance lithium ion batteries†

Jinlong Yang,‡[a,b] Jiaxin Zheng,‡[a] Lin Hu,[b] Rui Tan,[a] Kai Wang,[a] Shichun Mu*[b] and Feng Pan*[a]

A novel design based on both FeO$_x$ and Si nano-dots bonded with graphene (FeO$_x$·Si@GNS) as dual lithium-storage centers is reported. They show high performance as anode materials for Li-ion batteries with a remarkable reversible capacity of 1160 mA h g^{-1} at 0.2 A g^{-1}, fast charging/discharging rate, and long cycling life (*e.g.*, a capacity retention of 81.7% at 2.0 A g^{-1} after 600 cycles). The origin of these high performances comes from the key factors of the high theoretical specific capacity of FeO$_x$ and Si, the shorter Li-ion diffusion distance of both nano-dot structures, fast electron conductivity, and the strain relaxation due to volume variations of both nano-dots bonded with graphene nanosheets during cycles.

As important electrochemical energy storage devices, rechargeable Li-ion batteries (LIBs) are widely used for portable electronics and increasingly for hybrid electric vehicles (HEVs) and electric vehicles (EVs).[1] The cathode and anode materials of LIB as Li-storage centers operate by reversible lithiation and delithiation during charge and discharge. For anode materials, there are two kinds of Li-ion storage mechanisms: one is through intercalation/de-intercalation reactions, using the traditional graphite with a layered structure[2] and the newly interest-provoked structural Li$_4$Ti$_5$O$_{12}$ (LTO) with a spinel structure, and the other is through conversion reactions, using transition metal oxides and Si. Si,[3] SiO$_x$,[4] and transition metal oxides[5] are considered to be the most promising anode materials, due to the high theoretical specific capacity, such as 924 mA h g^{-1} for Fe$_3$O$_4$,[6] and 4200 mA h g^{-1} for Si.[7] However, these materials possess high irreversible capacity, low rate and poor cycling performance due to their low diffusion coefficient and conductivity, as well as the significant volume expansion and disintegration during the Li-ion extraction/insertion process. The volume expansion would lead to active particle cracking, electrode pulverization, and subsequent loss of electrical contact between the active material and current collector,

resulting in poor reversibility and rapid capacity fading, especially at high current densities. To overcome these problems, several strategies have been proposed, which include the construction of nanostructured materials,[8] functional-coating materials,[9] and heterostructure materials.[10] On the other hand, nearly all previous studies about the above anode materials are based on one kind of active material for Li-ion storage, namely one-active-center mechanism in those studies. Designing an anode material which combines two kinds of active materials for Li-ion storage would be an interesting topic for fundamental research and real applications of Li-ion batteries. To the best of our knowledge, almost no work about this has been reported.

Graphene nano-sheets (GNS), about one to five layer-thick sheets of a honeycomb carbon lattice, exhibit high conductivity, light weight, high mechanical strength, structural flexibility, and large surface area.[11] Graphene was widely used in hybrid nanocomposites for electrode materials, such as Fe$_3$O$_4$–graphene[6] and Si–graphene nanocomposites,[12] to improve the electrochemical performance. Firstly, the ultrathin graphene sheets can act as a barrier to prevent the aggregation of nanoparticles and enhance the cycling performance. Secondly, the porous graphene sheets can provide void space against the volume changes of the particles during the lithium ion insertion/extraction process, which can improve the cycling performance. Thirdly, the graphene sheets themselves are active materials for additional Li$^+$ storage (3–5 layer capacity about 450 mA h g^{-1}),[13] which is of great benefit to the reversible specific capacity. Finally, the nanoparticles are anchored on the surface of the graphene sheets, which can lead to a high rate performance due to the high electronic conductivity of

[a]School of Advanced Materials, Peking University Shenzhen Graduate School, Shenzhen 518055, China. E-mail: panfeng@pkusz.edu.cn
[b]State Key Laboratory of Advanced Technology for Materials Synthesis and Processing, Wuhan University of Technology, Wuhan 430070, China. E-mail: msc@whut.edu.cn
†Electronic supplementary information (ESI) available. See DOI: 10.1039/c5nr03311j
‡These authors contributed equally to this work.

graphene sheets and short path length for Li$^+$ transport of nanoparticles. Therefore, it is believed that such anode nanocomposites with graphene can possess a large reversible specific capacity, long cycling life, and good rate capability.

Herein we for the first time synthesized a novel anode sandwich-nanosheet material, FeO$_x$·Si@GNS, with activated FeO$_x$ and Si nano-dot domains bonded with graphene as dual lithium-storage centers. Due to the high theoretical specific capacity for the dual centers of FeO$_x$ and Si, the hybrid composite shows a high reversible capacity of 1160 mA h g^{-1} at 0.2 A g^{-1} as an anode material. Apart from this, it also shows large-current and long-life performance (a capacity retention of 81.7% at 2.0 A g^{-1} after 600 cycles). This hybrid composite is prepared as follows: we first anchored Li$_2$FeSiO$_4$ nanorods (LFSNRs) onto GNS (LFSNR@GNS), and after initial cycling (lithiation/delithiation), the LFSNR@GNS evolves into a 2D hybrid sheet material with activated FeO$_x$ and Si nanodot domains bonded with graphene. This novel anode material with FeO$_x$ and Si nano-dot domains anchored on GNS provides a short Li-ion diffusion distance and large contact surface with the electrolyte, and also accommodates the volume variations to relax the strain by GNS during lithiation/delithiation. Besides this, GNS can improve the electron conductivity to enhance the depolarization effect and hold FeO$_x$ and Si to prohibit them from accumulation so as to enhance Li-ion transportation. All the above factors enable the excellent electrochemical performance for the novel designed anode.

The hybrid material of FeO$_x$·Si@GNS is generated by the electrochemical reaction of LFSNR@GNS. The synthesis routes and related mechanisms are illustrated in Schemes 1 and 2. The LFSNR@GNS is synthesized according to the following steps, which are also reported in our previous work.[14] First, graphene oxide nanosheets (GONS) were synthesized from natural graphite flakes using a modified Hummers' method[15] (Scheme 1a). And then LFSNR was obtained *via* a hydrothermal method of a suspension with a 4 : 1 : 1 : 0.5 molar ratio of LiOH, TEOS (ethyl orthosilicate), Fe(NO$_3$)$_3$·9H$_2$O, and
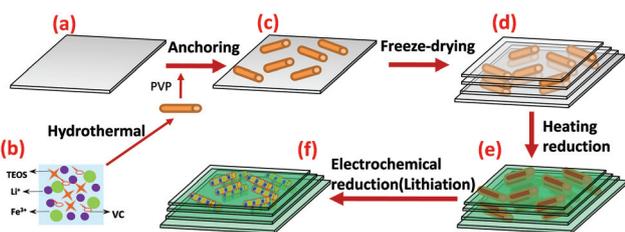
Scheme 1 Schematic fabrication process for the multilayered hybrid material: (a) substrate material GONS, (b) synthesis of LFSNRs in a water/ethylene glycol mixture at 200 °C for 6 days, (c) nanorods anchored on the surface of GONS using PVP modification, (d) 2D multi-layered sandwich structure with alternating LFSNR layers and GO layers obtained through freeze drying, (e) 2D multi-layered sandwich structure with alternating LFSNR layers and GNS layers obtained through thermal reduction at 600 °C for 6 h under a flow of N$_2$, (f) 2D multi-layered sandwich structure with Fe(Li$_2$O) and Li$_y$Si nano-dots dual Li-storage centers and GNS layers obtained through electrochemical reduction (lithiation).
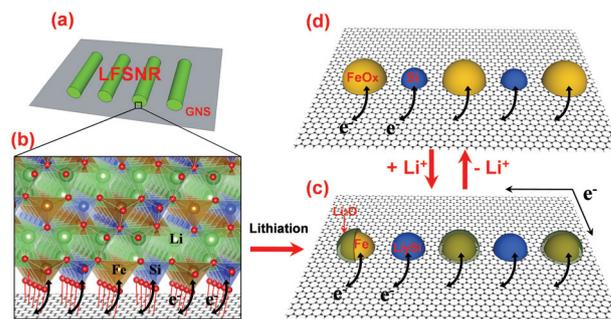
Scheme 2 Schematic representation of the structural change of 2D hybrid sheets (Scheme 1e) in the electrochemical process: (a) initial 2D hybrid structure, (b) enlarged illustration shows the crystal structure of LFSNRs and bonding of graphene with alternate FeO$_4$ and SiO$_4$ tetrahedra, (c) lithiation structure (Scheme 1f) with dual Li-storage centers (at 0.001 V) and (d) cycle structure (at 3 V) of FeO$_x$ and Si nano-dot centers bonded with graphene (FeO$_x$·Si@GNS).

vitamin C (VC) in a 5 : 1 volume ratio of water/ethylene glycol (EG) at 200 °C for 6 days (Scheme 1b). VC and EG were not only used as reducing agents but also as solvents with good coordinating ability, which play a critical role in connection with precursors by van der Waals interactions and also as ligands to form coordination complexes with iron ions. This promotes the preferred nano-rod orientation growth of crystals. Subsequently, the prepared LFSNRs were modified by PVP to be anchored on the surface of GONS in aqueous solution (Scheme 1c). After freeze drying, the suspension restacked from single GONS to form 2D multi-layered sandwich structures (Scheme 1d) with LFSNRs embedded. Then such hybrid sandwich structures were heated and reduced at 600 °C for 6 h under a flow of N$_2$ to obtain the 2D multi-layered sandwich structures (Scheme 1e) with LFSNR@GNS. The single-layered LFSNR@GNS in sandwich is shown in Scheme 2a and b. After initial electrochemical reduction (lithiation), Fe(Li$_2$O) and Li$_y$Si nano-dot centers bonded with graphene (Scheme 1f and 2c) are formed. Then they are changed to FeO$_x$ and Si nano-dot centers bonded with graphene (FeO$_x$·Si@GNS) (Scheme 2d) after the reversible delithiation.

To demonstrate the above schemes, different tests were performed to characterize the two important products of Scheme 1e (LFSNR@GNS hybrid sheets) and 2d (FeO$_x$·Si@GNS). Fig. 1a shows the SEM image of the LFSNR@GNS hybrid sheets with a diameter of ~10 μm and thickness of ~200 nm. Specially, GNS in the 2D hybrid sheets was curled to form the rugged surface due to the strong anchoring effect between LFSNR and the surface of GNS. The GNS layers covered on the surface of LFSNR are shown in Fig. 1b. It can be seen that LFSNRs are homogeneously dispersed and fully encapsulated by continuous GNS films. The curled GNS layers and LFSNRs generate the sandwich structures to prevent LFSNRs from aggregation during the annealing process. From Fig. 1c, macropores with sizes of ~400 nm are found to exist in the hybrid sheets, which facilitate the electrolyte penetration. The TEM images of hybrid sheets reveal that the nanorods are
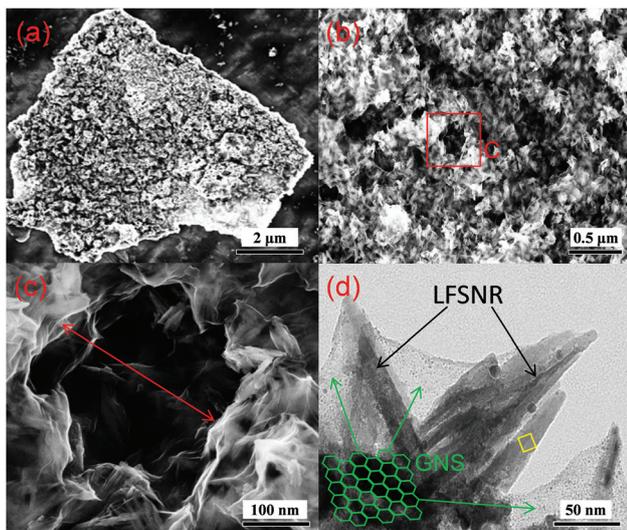
Fig. 1 SEM and TEM morphology characterization of the 2D hybrid nanostructures (Scheme 1e): (a) size and surface morphology characteristics of the 2D hybrid sheets, (b) GNS layers covered on the surface of LFSNRs, (c) macropore structure and GNS layers in the 2D hybrid sheet, (d) morphology and size of LFSNRs embedded in graphene after heating reduction.

Fig. 2 Detailed structures of graphene and chemical bonding in the hybrid nanosheets (Scheme 1e): (a) multilayered graphene and single nanorods embedded in graphene, (b) oxygen-containing functional groups including C=C, C–O, C=O and C=O–O at binding energy of C 1s, (c) Raman signals at the D (disordered) band and the G (graphite) band of sp^2 and sp^3 carbon structures in the hybrid.

embedded in GNS (Fig. 1d), and their morphologies and sizes (length of 200–300 nm, diameter of 10–25 nm) are the same as that of pristine LFSNRs (Fig. S1†) obtained by a hydrothermal process, which means the nanorods maintain their geometries after heat treatment.

The interfacial structures between graphene and LFSNRs of the LFSNR@GNS hybrid nanosheets are directly demonstrated by using magnified TEM images, X-ray photoemission spectroscopy (XPS), and Raman spectroscopy. The GNS layer can be easily observed from its wrinkles around LFSNRs, and the GNS shows 3–5 layers of graphene (Fig. 2a). At binding energy (B.E.) of C 1s (Fig. 2b), the chemical bonds are mainly oxygen-containing functional groups[18] including C–O, C=O, and C=O–O, indicating that the LFSNR could be chemically cross-linked with graphene by –C–O–Fe, –C–O–Li, and –C–O–Si bonds. The Raman signals (Fig. 2c) at around 1350 cm^{-1} (peak 2) and 1590 cm^{-1} (peak 4) are the D (disordered) band and the G (graphite) band of sp^2 type carbon-based materials, while the others at around 1180 cm^{-1} (peak 1) and 1510 cm^{-1} (peak 3) are related to sp^3 type carbon.[17] The integrated area ratio of sp^2 and sp^3 (A_{sp^2}/A_{sp^3}) can be used to roughly estimate the relative content of the graphite carbon. For our samples, the high A_{sp^2}/A_{sp^3} ratio (2.5) corresponding to a high content of sp^2 type structure is attributed to graphene in the hybrid. More importantly, the I_D/I_G ratio (the intensity ratio of D and G bands can be used to evaluate the graphitization degree) is fitted to 1.26, which is higher than the value of 1.17 for pure GNS (Fig. S2†). Hence, Raman spectroscopy of the hybrid nanosheet shows that there are more defects on GNS of LFSNR@GNS than that of the same GNS without LFSNRs,
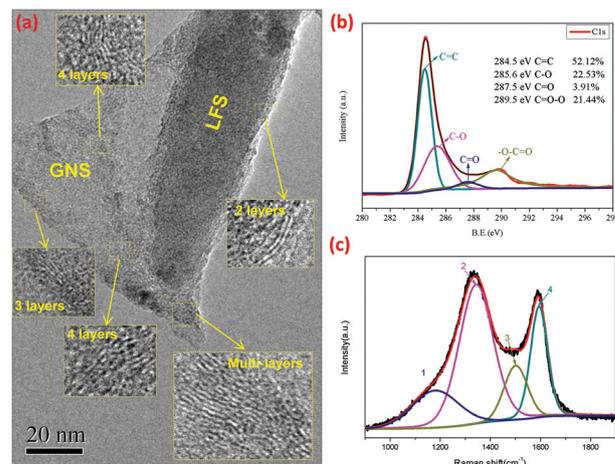
which can indirectly indicate the existence of chemical bonds at the interface of LFSNR@GNS.

Fig. 3a shows high resolution transmission electron microscopy (HRTEM) image of the hybrid (Scheme 1e). The discontinuous layers of the crystal with amorphous materials present at the edge of LFSNRs and close to graphene further implies that a type of chemical bonding between LFS and graphene was generated. The interplanar distance is 0.53 nm
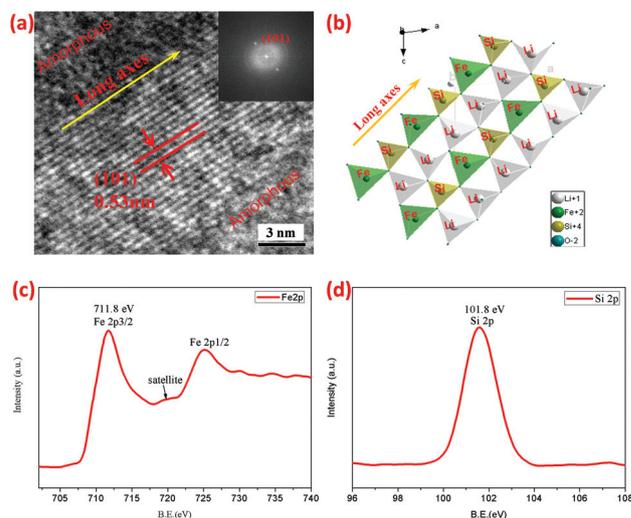

Fig. 3 Crystal structure in the hybrid (Scheme 1e): (a) high resolution transmission electron microscopy (HRTEM)(corresponding to the yellow line, "□" region in Fig. 1d), (b) FeO₄ and SiO₄ tetrahedra in the long axes direction are mutually alternate, and in the vertical direction of the long axis are separated by LiO₄ tetrahedra, (c) binding energy at Fe 2p, (d) binding energy at Si 2p.

corresponding to the (101) face of LFSNRs, and the long axes of the nanorods are perpendicular to the <101> direction. The atomic arrangement (Fig. 3b) in the LFSNR, viewed down the zone [010] axis, matches the expected structure for the monoclinic lattice (Fig. S3†) with the space group $P2_1/n$.[16] The FeO_4 and SiO_4 tetrahedra in the long axes direction are mutually alternate and are separated by LiO_4 tetrahedra in the vertical direction of the long axis, facilitating the formation of the FeO_x and Si nano-dots shown in Scheme 2c and d. Fe $2p^{2/3}$ B. E. (Fig. 3c) at 711.8 eV is consistent with the B.E. of Fe^{2+}.[19] Si 2p B.E. (Fig. 3d) at 101.8 eV is in line with Si^{4+} in polysiloxane.[20] When the LFSNR@GNS hybrid material is used as an anode, Fe^{2+} could be reduced to Fe^0,[21] Si^{4+} to Si^0 and further to form an Li_xSi alloy[22] after the lithiation reaction.

To further characterize the formation of $FeO_x \cdot Si@GNS$ dual lithium-storage centers through the electrochemical redox reaction (lithiation/delithiation) in Scheme 2, cyclic voltammetry (CV) (Fig. 4a) was performed in a voltage range of 0.001–3 V (vs. Li^+/Li) at a sweep rate of 0.2 mV s^{-1}, starting at the open circuit potential of 2.98 V. During the initial lithiation (first cycle, given in Scheme 2b and c) process, there are four broad peaks at 1.69, 1.05, 0.48 and 0.1 V: the weak peak at 1.69 V can be attributed to the irreversible reaction with the electrolyte corresponding to the formation of SEI layers;[23] the middle at

1.05 V may be associated with the lithiation reaction of LFSNRs; the lower at 0.48 V represents irreversible processes such as reduction of LFSNRs and consumption of lithium ions by oxygen-containing functional groups on GNS;[24] the lowest at 0.1 V may be the lithiation of the Li_ySi alloying reaction.[25] After the first cycling, the anode can do reversible lithiation/delithiation and maintain stable charge/discharge capacities. For example, in the second cycle, the reversible anodic peaks are mainly located at ≈0.5, 0.95, and 2.1 V, and cathodic peaks at 1.2, 0.84, 0.35, and ≈0.1 V, which are very complex and could be related to the reversible redox of FeO (Fe), alloying of Si (Li_ySi), intercalation as well as surface reaction of graphene, and so on. Fig. 4b shows the comparison among the CV curves of pristine GNS and LFSNRs. It can be found that the current peaks at 0.35/0.5 V are the graphite intercalation of GNS (eqn (1)),[27] and peaks at 0.84/0.95 V represent surface reaction related to the bond of –graphene–C–O–Li (eqn (2)),[24] whose intensities increase with the increased number of interfacial bonds of graphene with FeO_x and Si nano-dots. In addition, the peaks at 1.2/2.1 V correspond to the reduction of FeO_x and the oxidation of Fe (eqn (3)).[21] The current peak at 0.1 V is attributed to the alloying of Si, and the corresponding oxidation peak is at 0.26 V (eqn (4)).[22]

$$6C + Li^+ + e^- \leftrightarrow LiC_6 \quad (1)$$

$$Graphene\text{–}C\text{–}O\text{–} + Li^+ + e^- \leftrightarrow Graphene\text{–}C\text{–}O\text{–}Li \quad (2)$$

$$FeO_x + 2xLi^+ + 2xe^- \leftrightarrow Fe + xLi_2O \quad (3)$$

$$Si + yLi^+ + ye^- \leftrightarrow Li_ySi \quad (4)$$

From above structural and electrochemical analysis, the generation of FeO_x and Si nano-dots as well as the mechanism of dual Lithium storages can be attributed to interfacial structure with –C–O–Fe and –C–O–Si chemically bonding between the LFSNR and GNS, which was generated during syntheses (Scheme 2a and b), while graphene oxided nanosheets with C–O and –COO groups are reduced to graphene in the same process. The FeO_4 and SiO_4 tetrahedra in LFSNR crystals[28] are mutually alternate; step 2, after initial lithiation, Fe and Li_xSi nano-dot centers are formed (Scheme 2c), and then they are further changed to FeO_x and Si nano-dot centers bonded with graphene ($FeO_x \cdot Si@GNS$) after the reversible delithiation (Scheme 2d); step 3, in and after the second cycle, reversible lithiation/delithiation will cycle between FeO_x and $Fe(Li_2O)$ and between Si and Li_ySi (Scheme 2c and d), during which the $FeO_x \cdot Si$ (charged to 3 V) and $Fe(Li_2O) \cdot Li_ySi$ (discharged to 0.001 V) nano-dots are also observed by the XRD test (Fig. S4†).

The components and microstructure of the hybrid after electrochemical reduction were further investigated by the EDX spectrum and HRTEM. As shown in the TEM of Fig. 5a, the nano-dots are encapsulated by some films. The element mappings in Fig. 5b–f further ensure that the nano-dots are assigned to Fe and Si elements, the observed films belong to the C element of graphene, and the highly fragmented O element mapping indicates the connective function between the $FeO_x \cdot Si$ nano-dots with graphene. The HRTEM image in
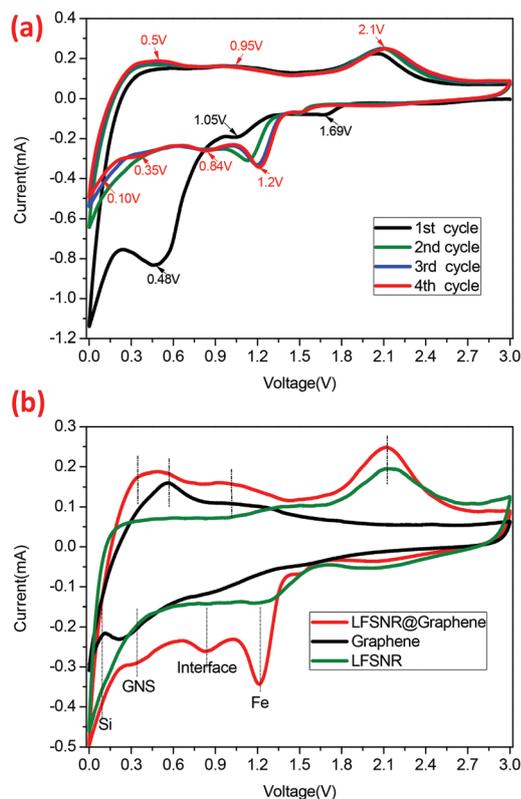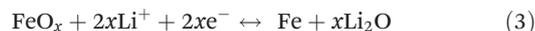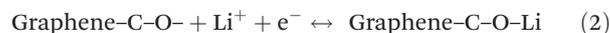

Fig. 4 (a) Cyclic voltammetry curves of the 2D hybrid sheets from 3.0 V to 0.001 V vs. Li/Li$^+$ in the first four-cycles at a scan rate of 0.2 mV s^{-1}, (b) stable cyclic voltammetry curves of the 2D hybrid sheets compared to pristine LFSNR and GNS electrodes.
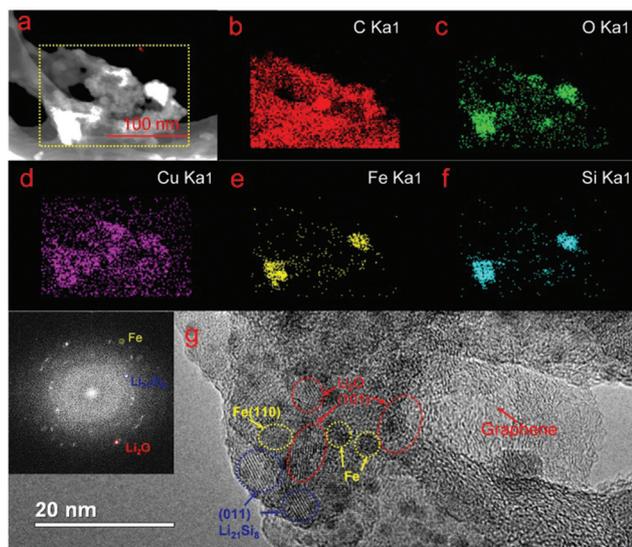
Fig. 5 (a) TEM image, (b−f) EDX spectra and (g) HRTEM image of the hybrid after electrochemical reduction (inset of g corresponds to the FFT image).

Fig. 6 (a) Cyclic voltammetry curves of the 2D hybrid sheets at different current rates from 0.2 to 0.6 mV s^{-1}. (b) The b-values (from the slope of the peak current *versus* the potential scan rate on a logarithmic scale in Fig. S5†) corresponding to different electrochemical centers in the FeO$_x$·Si@GNS hybrid.

Fig. 5g shows the microstructure with abundant Fe(Li$_2$O)·Li$_y$Si nano-crystals embedded around graphene as the hybrid structure after electrochemical reduction, which correspond to the description in Scheme 2c.

Cyclic voltammetry with varying sweep rates (Fig. 6a) of the FeO$_x$·Si@GNS is carried out to investigate the electrochemical transport kinetics that mainly include semi-infinite linear diffusion control related to the reactive species and the charge transfer control without being limited by the current rate.[26] It is commonly accepted that the current peak related to Li extraction/insertion in a sweep voltammetry experiment obeys a power-law relationship with the sweep rate which leads to:[26] $i = a\nu^b$, where i is the current (A), ν is the potential sweep rate (V s^{-1}), and a and b are the arbitrary coefficients. Whereas the b-value of 0.5 indicates that the current is controlled by semi-infinite linear diffusion, and the value of 1 indicates that the current is surface-controlled. Fig. S5† shows the change of the peak current (arrow marks) *versus* the potential scan rate on a logarithmic scale. The b-values (Fig. 6b) of the FeO$_x$·Si@GNS at 0.1, 0.35, 0.5, 0.84, 0.95, 1.2, and 2.1 V are all between 0.5 and 1, indicating a concurrence of both lithium semi-infinite linear diffusion and surface reactions. Specially, the b-values (0.896/0.894) of the surface reaction related to the bond of –graphene–C–O–Li are close to 1, corresponding to a special electrochemical behavior of pseudocapacitance.[26]

The typical charge–discharge curves of the hybrid sheets as an anode cycled at 0.02 A g^{-1} between 0.001 and 3 V (*vs.* Li$^+$/Li) are shown in Fig. 7a. The thicknesses and densities of the electrodes in this work were similar to those of commercial carbon electrodes (about 100 μm and 10 mg cm^{-2}).[30] The 1st specific discharge capacity of the hybrid is up to 1810 mA h g^{-1}. Subsequently, the 2nd specific discharge capacity decreases to
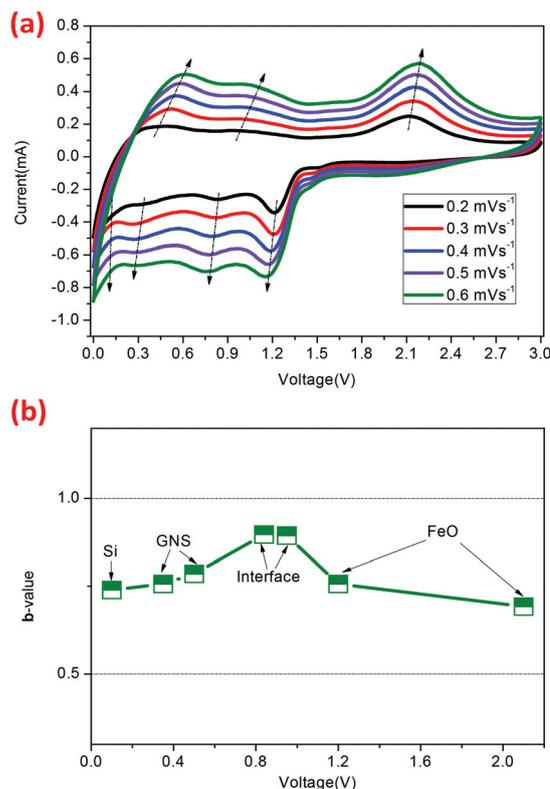
1160 mA h g^{-1} with the capacity retention ratio about 64.08%. The first part of the irreversible capacity loss can be attributed to the Si^{4+} of Li$_2$FeSiO$_4$ which is reduced to Si^0. The second part is from the formation of solid electrolyte interface (SEI) films of the cycling of Fe@FeO$_x$ and Si@Li$_y$Si in the charging/discharging, which is similar to that of transition metal oxides.[5]

The specific capacity is maintained at above 1000 mA h g^{-1} after 20 cycles. In the hybrid, because the content of graphene is only 6.9 wt% as shown in the ESI and Fig. S6,† the capacity contribution is mainly attributed to Fe@FeO$_x$ and Si@Li$_y$Si, in which FeO$_x$ and Si are the most promising elements with high theoretical specific capacity as anodes for lithium ion batteries.

In contrast, pristine GNS reduced by the same graphene oxide shows a discharge specific capacity of 570 mA h g^{-1} at 0.02 A g^{-1} (Fig. S7†), while pristine LFSNRs prepared using the same process but without the presence of GNS shows a discharge specific capacity of 630 mA h g^{-1} at 0.02 A g^{-1} (Fig. S8†). The much higher specific capacity of the hybrid sheets should be attributed to the special hybrid structure with chemical bonds at the interfaces of GNS/FeO$_x$ and GNS/Si, which enables the high electrical conductivity and activates
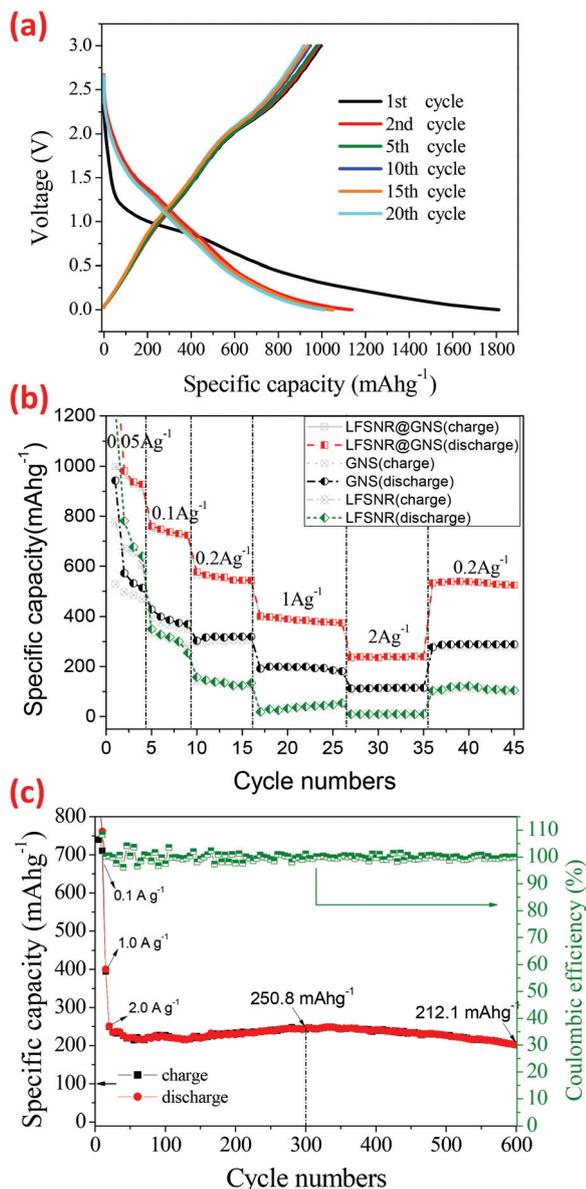
Fig. 7 Electrochemical characteristics: (a) galvanostatic charge/discharge profiles of the initial twenty cycles at 0.02 A g^{-1}. (b) Charge/discharge capacities at various current rates compared to pristine LFSNR and GNS electrodes. (c) Cyclic performance of 2D hybrid sheets cycled at 2 A g^{-1} for 600 cycles.

the dual-active-center Li-ion storage mechanism as shown in Scheme 2. Moreover, the rate capacities (Fig. 7b) of this hybrid material are much higher than that of these pristine materials. Fig. S9† shows the typical charge–discharge curves at various current densities between 0.001 and 3 V for the hybrid. The discharge specific capacities of 900, 760 and 600 mA h g^{-1} can be obtained at the charging/discharge current densities of 0.05, 0.1 and 0.2 A g^{-1}, respectively. Even at a charge and discharge current density of 2.0 A g^{-1}, it still retains a specific capacity of 240 mA h g^{-1}. Furthermore, the hybrid anode also shows excellent cycling performance at a high current density.

As shown in Fig. 7c, the highest discharge specific capacity is 250.8 mA h g^{-1} at 2.0 A g^{-1} within 300 cycles, and the capacity still remains 212.1 mA h g^{-1} after 600 cycles, corresponding to the capacity retention of 81.7%. This demonstrates the excellent electrochemical stability of the 2D hybrid sheets. The SEM and HRTEM images (Fig. S10†) after long cycles show a micron grade of the block structure with FeO$_x$ and Si nanocrystals fixed on the surface of GNS indicating high structural stability.

The high storage capacity, high rate capability, and good cycling ability of the novel 2D hybrid anode can be attributed to the dual-active-center with a high theoretical specific capacity of Si and FeO$_x$ nano-dots, good electrical conductivity of GNS, and the unique hybrid structure. Here the chemical bonded interface in the hybrid would not only lead to easier charge transfer than the physical van der Waals interaction, but also can anchor the FeO$_x$ and Si nano-dots to prohibit them from accumulation during the charge/discharge (Scheme 2c and d). As a result, both FeO$_x$ and Si nano-dot domains (dual-active-centers) are activated for lithium ion storage. While the side part of GNS without FeO$_x$ and Si nano-dots could be reconstructed to form the 2D graphite structure due to van der Waals forces, providing mechanical stability and accommodating the volume change during lithiation/delithiation to ensure the reversible cycling stability.[29] However, the initial coulombic efficiency of the hybrid sheets is similar to lots of previous studies using a metal oxide/graphene composite as an anode material. Hence, in-depth investigation should be conducted to raise the initial coulombic efficiency and to understand how to add an external Li source on anodes or cathodes effectively for practical application with full cells.

In summary, we for the first time report a novel anode material with activated FeO$_x$ and Si nano-dot domains bonded with graphene as dual lithium-storage centers. When cycled as anode materials, they show a high reversible capacity, large-current, and long-life performance. The high capacity is mainly attributed to the dual-active-center Li-ion storage mechanism, in which both FeO$_x$ and Si nano-dots are activated for lithium ion storage with high specific capacities. The graphene cannot only enhance electron transport in FeO$_x$ and Si nano-dots through the chemical bonds (–C–O–Fe–, and –C–O–Si–), but also relax the strain due to the large volume variation during cycles, which improve both electrochemical activity and cycling life of the novel hybrid anodes. We believe that this novel material with a unique 2D hybrid structure is very promising for commercial applications that require high energy, long operating life, and excellent abuse tolerance.

Notes and references

1 (a) J. M. Tarascon and M. Armand, *Nature*, 2001, **414**, 359; (b) K. Kang, Y. S. Meng, J. Bréger, C. P. Grey and G. Ceder, *Science*, 2006, **311**, 977; (c) X. Xiao, P. Lu and D. Ahn, *Adv. Mater.*, 2011, **23**, 3911; (d) J. Hassoun and B. Scrosati, *Adv. Mater.*, 2010, **22**, 5198; (e) B. Scrosati, J. Hassoun and Y. K. Sun, *Energy Environ. Sci.*, 2011, **4**, 32875; (f) G. Jeong, Y. U. Kim, H. Kim, Y. J. Kim and H. J. Sohn, *Energy Environ. Sci.*, 2011, **4**, 1986.

2 (a) M. Yoshio, H. Wang and K. Fukuda, *Angew. Chem., Int. Ed.*, 2003, **115**, 4335; (b) M. Fujimoto, Y. Shoji, Y. Kida, R. Ohshita, T. Nohma and K. Nishio, *J. Power Sources*, 1998, **72**, 226.

3 N. Liu, K. Huo, M. T. McDowell, J. Zhao and Y. Cui, *Sci. Rep.*, 2013, 3.

4 K. Peng, J. Jie, W. Zhang and S. T. Lee, *Appl. Phys. Lett.*, 2008, **93**, 033105.

5 P. Poizot, S. Laruelle, S. Grugeon, L. Dupont and J.-M. Tarascon, *Nature*, 2000, **407**, 496.

6 G. Zhou, D.-W. Wang, F. Li, L. Zhang, N. Li, Z.-S. Wu, L. Wen, G. Q. Lu and H.-M. Cheng, *Chem. Mater.*, 2010, **22**, 5306.

7 M. Y. Ge, J. P. Rong, X. Fang and C. W. Zhou, *Nano Lett.*, 2012, **12**, 2318.

8 X. Zhu, Y. Zhu, S. Murali, M. D. Stoller and R. S. Ruoff, *ACS Nano*, 2011, **5**, 3333.

9 W.-M. Zhang, X.-L. Wu, J.-S. Hu, Y.-G. Guo and L.-J. Wan, *Adv. Funct. Mater.*, 2008, **18**, 3941.

10 W. Zhou, C. Cheng, J. Liu, Y. Y. Tay, J. Jiang, X. Jia, J. Zhang, H. Gong, H. H. Hng, T. Yu and H. J. Fan, *Adv. Funct. Mater.*, 2011, **21**, 2439.

11 (a) C. Lee, X. Wei, J. W. Kysar and J. Hone, *Science*, 2008, **321**, 385; (b) F. Liu, P. Ming and J. Li, *Phys. Rev. B: Condens. Matter*, 2007, **76**, 064120; (c) S. Bae, H. Kim, Y. Lee, X. Xu, J. S. Park, Y. Zheng and S. Iijima, *Nat. Nanotechnol.*, 2010, **5**, 574; (d) A. S. Mayorov, R. V. Gorbachev, S. V. Morozov, L. Britnell, R. Jalil, L. A. Ponomarenko, P. Blake, K. S. Novoselov, K. Watanabe, T. Taniguchi and A. K. Geim, *Nano Lett.*, 2011, **11**, 2396; (e) S. V. Morozov, K. S. Novoselov, M. I. Katsnelson, F. Schedin, D. C. Elias, J. A. Jaszczak and A. K. Geim, *Phys. Rev. Lett.*, 2008, **100**, 016602; (f) A. A. Balandin, *Nat. Mater.*, 2011, **10**, 569; (g) Y. Zhu, S. Murali, M. D. Stoller, K. J. Ganesh, W. Cai, P. J. Ferreira and R. S. Ruoff, *Science*, 2011, **332**, 1537.

12 J. Chang, X. Huang, G. Zhou, S. Cui, P. B. Hallac, J. Jiang, P. T. Hurley and J. Chen, *Adv. Mater.*, 2014, **26**, 758.

13 E. J. Yoo, J. Kim, E. Hosono, H. Zhou, T. Kudo and I. Honma, *Nano Lett.*, 2008, **8**, 2277.

14 J. Yang, L. Hu, J. Zheng, D. He, L. Tian, S. Mu and F. Pan, *J. Mater. Chem. A*, 2015, **3**, 9601.

15 (a) L. J. Cote, F. Kim and J. Huang, *J. Am. Chem. Soc.*, 2009, **131**, 1043; (b) D. P. He, K. C. Cheng, H. G. Li, T. Peng, F. Xu, S. C. Mu and M. Pan, *Langmuir*, 2012, **28**, 3979; (c) D. He, Y. Jiang, H. Lv, M. Pan and S. Mu, *Appl. Catal., B*, 2013, **132**, 379.

16 S. I. Nishimura, S. Hayase, R. Kanno, M. Yashima, N. Nakayama and A. Yamada, *J. Am. Chem. Soc.*, 2008, **130**, 13212.

17 (a) X. Zhou, F. Wang, Y. Zhu and Z. Liu, *J. Mater. Chem.*, 2011, **10**, 3353; (b) S. C. Mu, H. L. Tang, S. H. Qian, M. Pan and R. Z. Yuan, *Carbon*, 2006, **44**, 762.

18 (a) S. W. Lee, N. Yabuuchi, B. M. Gallant, S. Chen, B.-S. Kim, P. T. Hammond and Y. Shao-Horn, *Nat. Nanotechnol.*, 2010, **5**, 531; (b) A. Abouimrane, O. C. Compton, K. Amine and S. T. Nguyen, *J. Phys. Chem. C*, 2010, **114**, 12800.

19 J. Yang, X. Kang, L. Hu, X. Gong and S. Mu, *J. Mater. Chem. A*, 2014, **2**, 6870.

20 D. Rangappa, K. D. Murukanahally, T. Tomai, A. Unemoto and I. Honma, *Nano Lett.*, 2012, **12**, 1146.

21 (a) M. V. Reddy, T. Yu, C.-H. Sow, Z. X. Shen, C. T. Lim, G. V. SubbaRao and B. V. R. Chowdari, *Adv. Funct. Mater.*, 2007, **17**, 2792; (b) Y. Xu, Y. Li, S. Liu, H. Li and Y. Liu, *J. Power Sources*, 2012, **220**, 103.

22 W. S. Chang, C. M. Park, J. H. Kim, Y. U. Kim, G. Jeong and H.-J. Sohn, *Energy Environ. Sci.*, 2012, **5**, 6895.

23 J.-Z. Wang, C. Zhong, Da. Wexler, N. H. Idris, Z.-X. Wang, L.-Q. Chen and H.-K. Liu, *Chem. – Eur. J.*, 2011, **17**, 661.

24 (a) X. Han, G. Qing, J. Sun and T. Sun, *Angew. Chem., Int. Ed.*, 2012, **51**, 5258; (b) G. Wang, X. Shen, J. Yao and J. Park, *Carbon*, 2009, **47**, 2049.

25 L. Zhang, J. Deng, L. Liu, W. Si, S. Oswald, L. Xi, M. Kundu, G. Ma, T. Gemming, S. Baunack, F. Ding, C. Yan and O. G. Schmidt, *Adv. Mater.*, 2014, **26**, 4527.

26 (a) J. Come, V. Augustyn, J. W. Kim, P. Rozier, P. L. Taberna, P. Gogotsi and P. Simon, *J. Electrochem. Soc.*, 2014, **161**, A718; (b) V. Augustyn, J. Come, M. A. Lowe, J. W. Kim, P. L. Taberna, S. H. Tolbert and B. Dunn, *Nat. Mater.*, 2013, **12**, 518.

27 E. Peled, C. Menachem, D. Bar-Tow and A. Melman, *J. Electrochem. Soc.*, 1996, **143**, L4.

28 A. R. Armstrong, N. Kuganathan, M. S. Islam and P. G. Bruce, *J. Am. Chem. Soc.*, 2011, **133**, 13031.

29 J. K. Lee, K. B. Smith, C. M. Hayner and H. H. Kung, *Chem. Commun.*, 2010, **46**, 2025.

30 Y. Gogotsi and P. Simon, *Science*, 2011, **334**, 917.